catalysts

MDPI

Article

Reconstruction of $Bi_2O_2CO_3/Bi_2O_2SO_4$ Heterojunction Catalysts for the Reduction of Electrocatalytic CO_2 to Formate

Hongtao Xie [1,*], Limi Yan [1], Shijian Lu [1,*], Pengcheng Xiang [2,3], Dongliang Liu [3] and Lili Wang [2,3,*]

[1] Jiangsu Provincial Key Laboratory of Carbon Capture, Utilization and Storage, Carbon Neutrality Institute, China University of Mining and Technology, Xuzhou 221008, China; 18348286059@163.com
[2] College of Interdisciplinary Sciences, Liaoning University of Technology, Jinzhou 121001, China; xiangpengcheng1022@163.com
[3] Huzhou Key Laboratory of Smart and Clean Energy, Yangtze Delta Region Institute (Huzhou), University of Electronic Science and Technology of China, Huzhou 313001, China; dlliu@csj.uestc.edu.cn
* Correspondence: xieht@cumt.edu.cn (H.X.); lushijian@cumt.edu.cn (S.L.); wanglili20210525@163.com (L.W.)

Abstract

The electrocatalytic reduction of CO_2 into value-added chemicals offers a promising route to mitigate greenhouse gas emissions, yet the uncontrollable structural reconstruction and surface rearrangement of electrocatalysts during operation often lead to severe activity degradation. Herein, we reveal that $Bi_2O_2SO_4$ (BSO) undergoes an irreversible phase transformation into $Bi_2O_2CO_3$ (BCO) nanosheets accompanied by the partial reduction of Bi^{3+} to metallic Bi^0 under cathodic potentials. A series of BCO/BSO heterojunction catalysts with tunable compositions are synthesized via a mild in situ ion-exchange method. To circumvent the detrimental effects of this dynamic reconstruction, we devise a pre-activation strategy that deliberately completes the structural evolution prior to electrocatalysis. The optimized 20%-BCO/BSO heterojunction achieves a remarkable Faradaic efficiency of 98.4% for formate production in a flow cell at elevated potentials, with >95% $FE_{(HCOOH)}$ over a wide potential window (−0.8 to −1.7 V vs. RHE). In situ infrared spectroscopy elucidates that the reconstructed interface can promote CO_2 adsorption, stabilize the *OCHO intermediate, and facilitate HCOOH desorption. This work provides experimental evidence of the reconstruction behaviour of bismuth-based catalysts and offers a rational design method for constructing structurally stable heterojunction electrocatalysts.

Keywords: electrocatalytic reconstruction; CO_2 reduction; heterojunction catalysts; pre-activation; formate

Academic Editor: Sang-Il Choi

Received: 14 July 2026
Revised: 6 August 2026
Accepted: 8 August 2026
Published: 14 August 2026

1. Introduction

The relentless rise in atmospheric carbon dioxide (CO_2) concentration has emerged as one of the most pressing environmental challenges of the twenty-first century [1–3], necessitating the urgent development of efficient carbon capture, utilization, and storage (CCUS) technologies [4–6]. Among the diverse CCUS pathways, electrocatalytic CO_2 reduction (CO_2RR) powered by renewable electricity stands out as a particularly compelling strategy [7–10]. Unlike thermochemical or photocatalytic routes, electrochemical CO_2 reduction operates under ambient temperature and pressure, offers flexible control over reaction selectivity through the applied potential, and integrates seamlessly with intermittent renewable energy sources such as solar and wind power [11–13]. Moreover, the products of CO_2 electroreduction—including carbon monoxide, formic acid, methanol, methane,

ethylene, and ethanol—are valuable chemical feedstocks or fuels, thereby providing economic incentives alongside environmental benefits [14,15]. Nevertheless, the practical implementation of CO_2 electrolysis remains severely constrained by high overpotentials, limited product selectivity, and the competing hydrogen evolution reaction (HER), all of which are intimately linked to the intrinsic properties of the electrocatalyst. Consequently, substantial research efforts have been devoted to the rational design of earth-abundant, highly selective, and durable electrocatalytic materials [16–19].

Bismuth-based materials have garnered increasing attention as promising electrocatalysts for CO_2-to-formate conversion, owing to several advantageous features: low toxicity, high natural abundance, favorable binding energy with key reaction intermediates, and pronounced suppression of the competing HER [20–25]. Bismuth oxide (Bi_2O_3), metallic Bi, and various bismuth-based ternary compounds have all been explored for CO_2RR, with formate Faradaic efficiencies frequently exceeding 90% in optimized systems [22–25]. Angel Irabien et al. have made significant and well-established contributions to the development of Bi-based electrocatalysts and continuous electrochemical systems for CO_2-to-formate conversion [24,25]. Among these, bismuth oxysulfate ($Bi_2O_2SO_4$, BSO) has demonstrated a remarkable performance, attributable to its unique layered structure that facilitates ion transport and exposes abundant active sites [26]. However, a critical yet often overlooked aspect of bismuth-based electrocatalysts is their structural instability under operating conditions, as many of these materials undergo in situ phase transformations during electrolysis [27].

Despite the widespread observation of reconstruction phenomena in bismuth-based catalysts, the underlying mechanisms governing the phase transformation pathways remain insufficiently understood. More importantly, the pivotal question of how to harness rather than simply suppress reconstruction to achieve stable and highly active catalysts has yet to be systematically addressed. Conventional strategies have predominantly focused on inhibiting reconstruction through protective coatings or rigid frameworks, but these approaches typically compromise active site exposure and intrinsic catalytic activity [27,28]. In this context, heterojunction engineering offers a powerful means to modulate interfacial electronic structures and guide the reconstruction process in a controlled manner [28–31]. By constructing well-defined interfaces between two bismuth-based phases with complementary properties, it becomes possible to synergistically combine their respective advantages: one phase may provide structural stability while the other contributes high intrinsic activity [26]. Furthermore, the heterojunction interface can serve as a preferential site for reconstruction, directing the phase transformation toward a controlled and beneficial outcome.

In this work, we design a series of BCO/BSO heterojunction catalysts with tunable BCO contents via a mild in situ ion-exchange method, and subsequently stabilize the catalyst structure through a pre-activation strategy. The structural and morphological evolution of BSO under cathodic potentials is systematically characterized using XRD, SEM, TEM, and XPS, revealing a complete transformation into BCO nanosheets accompanied by the partial reduction of Bi^{3+} to metallic Bi^0. Combined with in situ ATR-FTIR spectroscopy, we identify the key reaction intermediates and elucidate the plausible reaction pathway. The optimized 20%-BCO/BSO catalyst achieves an outstanding formate Faradaic efficiency of 98.4% at −1.2 V vs. RHE in a flow cell. This work not only elucidates the reconstruction mechanism but also provides a practical pre-activation strategy that transforms structural instability into a beneficial factor for stable and efficient CO_2 electroreduction.

2. Results and Discussion

2.1. Structural Characterization of As-Prepared Catalysts

The crystal structures of the as-synthesized BCO/BSO heterojunction samples with different Na_2CO_3 additions were first examined by XRD, as shown in Figure 1. The pristine BSO precursor exhibits a set of characteristic diffraction peaks at 2θ = 13.1°, 21.9°, 28.8°, 39.9° and 50.8°, which are indexed to the standard pattern of monoclinic BSO (JCPDS 41-0688) [26]. With the gradual addition of Na_2CO_3 solution, new diffraction peaks emerge at 2θ = 13.1°, 23.9°, 26.2°, 30.2°, and 32.7°, which perfectly match the standard diffraction pattern of tetragonal $Bi_2O_2CO_3$ (JCPDS 41-1488) [32], corresponding to the (002), (101), (004), (103) and (110) crystal planes. The intensities of these BCO peaks progressively increase with increasing Na_2CO_3 addition, while the BSO peaks diminish correspondingly. When the added Na_2CO_3 reaches the stoichiometric equivalent of 20 mL, the diffraction pattern shows only the characteristic peaks of BCO, confirming the complete phase conversion.

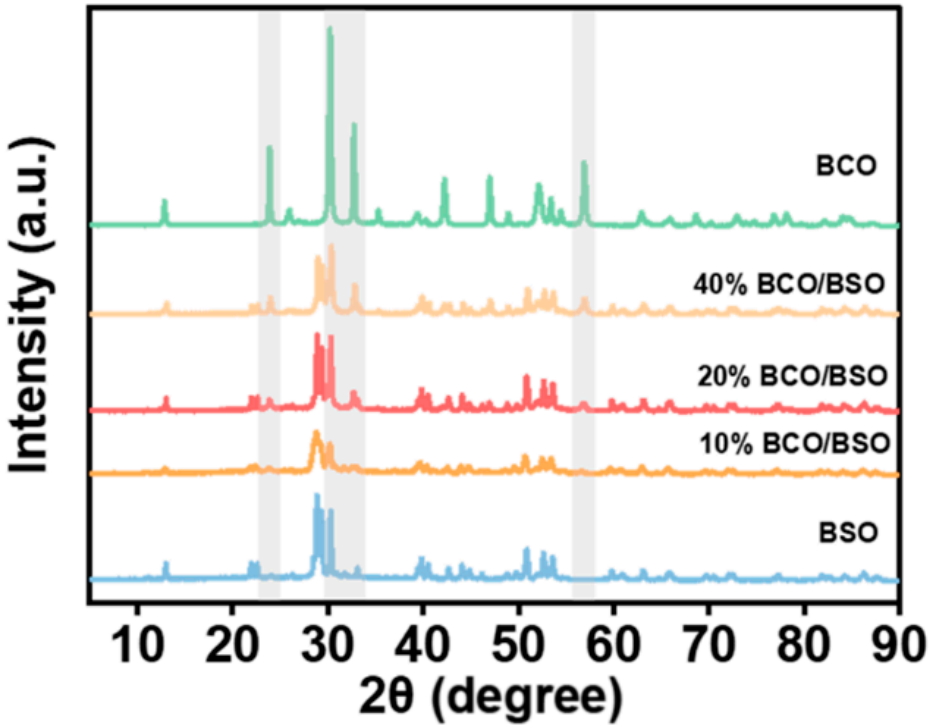

Figure 1. XRD patterns of pristine BSO, 10% BCO/BSO, 20% BCO/BSO, 40% BCO/BSO, and BCO.

The morphological evolution of the catalysts was examined by SEM, as presented in Figure 2. The pristine BSO exhibits irregular block-like particles with relatively smooth surfaces and dimensions ranging from several-hundred nanometres to a few micrometres (Figure S1). After treatment with 10% Na_2CO_3 (Figure 2a), the surface of the BSO particles becomes noticeably rougher, with the emergence of numerous nanosheet-like protrusions that appear to grow preferentially on certain crystal facets. At 20% Na_2CO_3 addition (Figure 2b), these protrusions develop into well-defined nanosheets that partially cover the substrate of nanoparticles. The nanosheets exhibit a thin, wrinkled morphology, characteristic of two-dimensional bismuth-based layered materials. With a further increase to 40% Na_2CO_3 (Figure 2c), the nanosheets become more densely packed and cover most of the substrate surface, while the underlying BSO blocks become less visible. Finally, the pristine BCO sample (Figure 2d) displays thicker homogeneous nanosheets, confirming the complete transformation. This gradual morphological evolution, from isolated protrusions to extensive nanosheet coverage, is fully consistent with the XRD results and demonstrates

that the BCO phase grows epitaxially on the BSO surface through the in situ ion-exchange reaction.

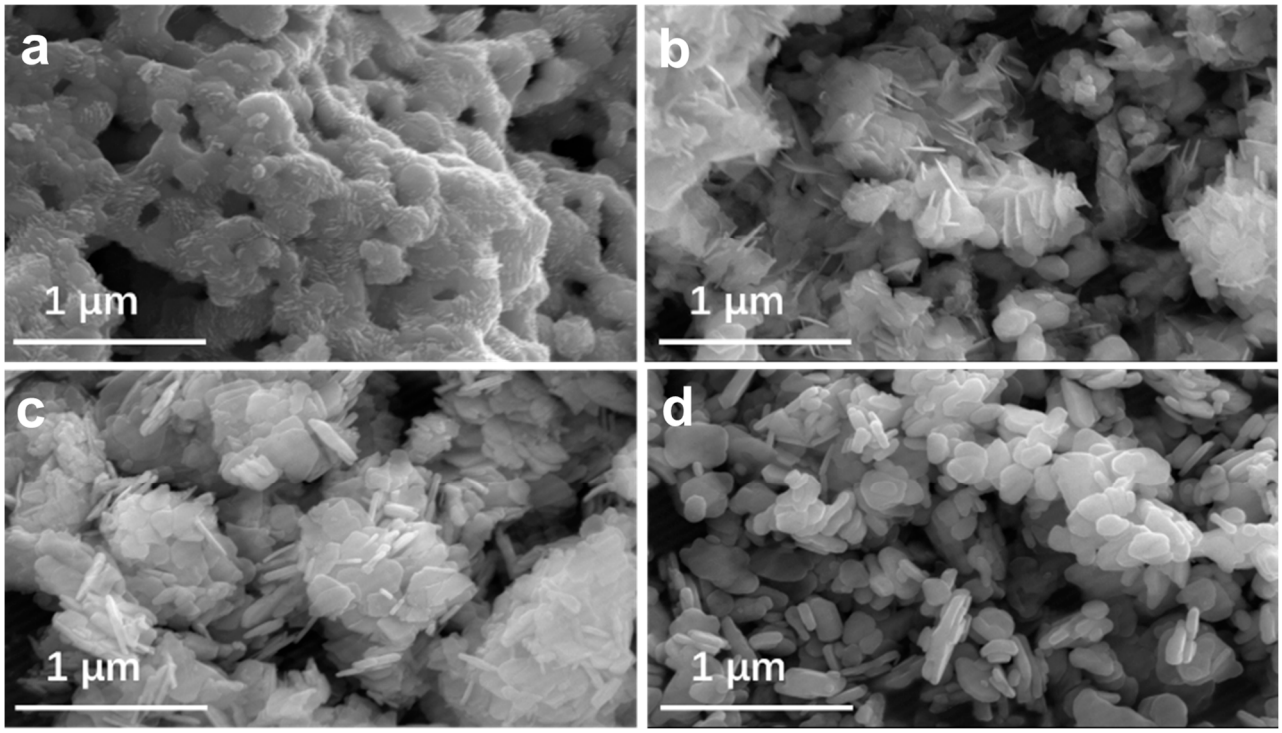

Figure 2. SEM images of (**a**) 10% BCO/BSO; (**b**) 20% BCO/BSO; (**c**) 40% BCO/BSO; (**d**) BCO.

2.2. Structural Evolution During Electrochemical Activation

To simulate the reconstruction that occurs under operating conditions, the as-prepared catalysts were subjected to electrochemical activation by cyclic voltammetry in CO_2-saturated 0.5 M $KHCO_3$. The XRD patterns of the activated samples are displayed in Figure 3. Remarkably, all heterojunction samples—regardless of their initial BCO content—exhibit essentially identical diffraction patterns after activation, dominated by the characteristic peaks of BCO (JCPDS 41-1488) at 2θ = 13.1°, 23.9°, 26.2°, 30.2°, and 32.7°. The characteristic peaks of the parent BSO phase (at 2θ = 28.9°, 39.9°) are completely absent, indicating that the BSO component has been entirely converted to BCO during the electrochemical process. This finding demonstrates that the reconstruction is primarily driven by the electrochemical environment (the applied cathodic potential and the carbonate-containing electrolyte) rather than the initial phase ratio. In addition to the BCO peaks, weak diffraction signals attributable to metallic bismuth (Bi^0) are discernible at 2θ = 27.2°, 37.9°, and 39.6°, which match the standard pattern of rhombohedral bismuth (JCPDS 44-1246) [33], corresponding to the (012), (104), and (110) crystal planes. The presence of metallic Bi indicates that a fraction of Bi^{3+} species underwent reduction during the cathodic polarization, likely facilitated by the locally reducing microenvironment created by the electric field at the electrode surface.

The morphological changes accompanying this phase transformation were revealed by SEM imaging of the activated samples (Figure 4). Prior to activation, the heterojunction samples exhibit a mixed morphology of BSO blocks with BCO nanosheets. After activation, all samples transformed into ultrathin nanosheet networks with a three-dimensional porous architecture, regardless of their original composition. The nanosheets appear highly flexible and interconnected, forming a flower-like or coral-like structure with abundant open pores. Notably, the complete conversion of BSO to BCO and the formation of the nanosheet

morphology occur within the first few CV cycles, suggesting that the reconstruction is kinetically fast under the applied conditions.

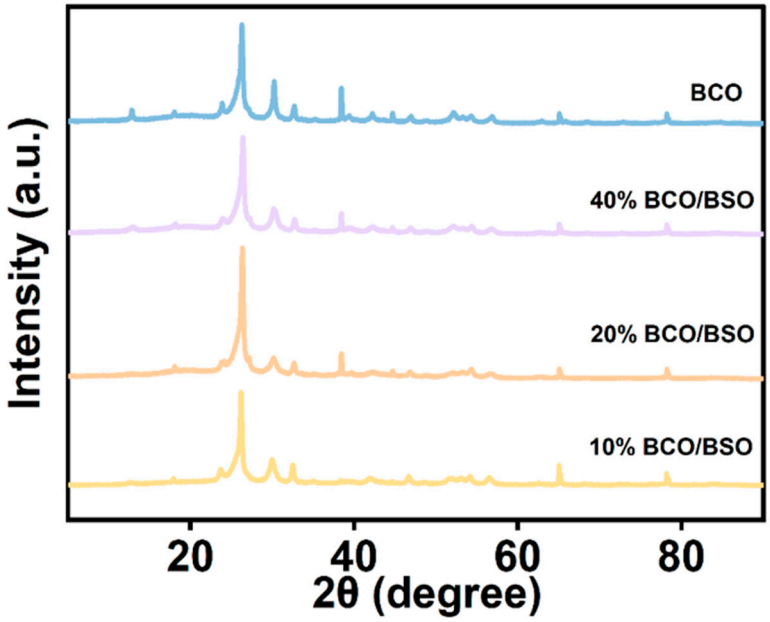

Figure 3. XRD patterns of pristine 10% BCO/BSO, 20% BCO/BSO, 40% BCO/BSO, and BCO after electrochemical activation.

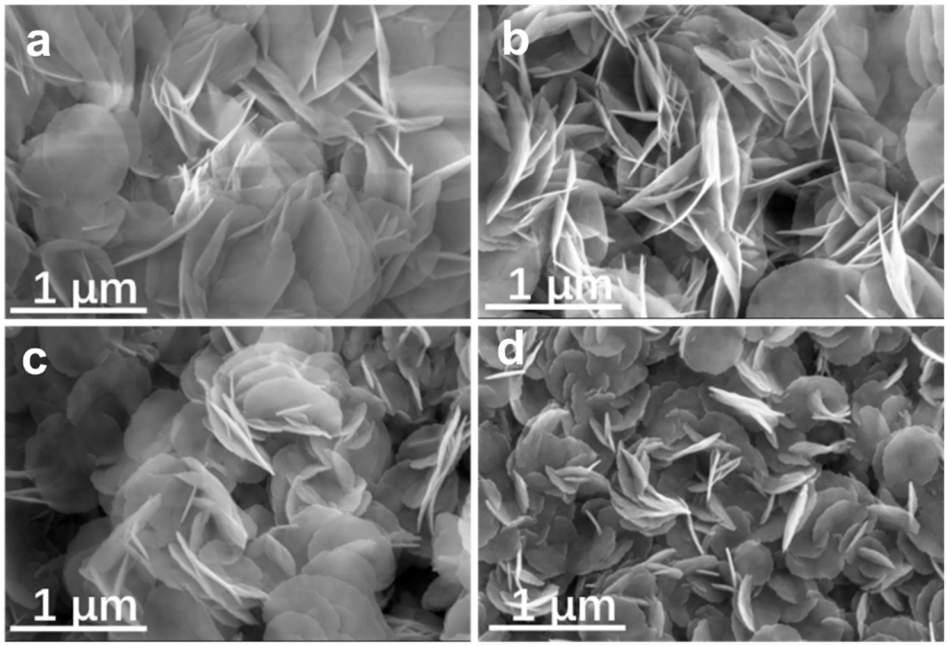

Figure 4. SEM images of pristine (**a**) 10% BCO/BSO, (**b**) 20% BCO/BSO, (**c**) 40% BCO/BSO, and (**d**) BCO after electrochemical activation.

To gain a deeper insight into the nanoscale structure of the activated catalyst, TEM and HRTEM images were taken of the activated 20%-BCO/BSO sample, as shown in Figure 5. The low-magnification TEM image (Figure 5a) confirms the three-dimensional nanoflower-like morphology, consisting of numerous ultrathin nanosheets. The HRTEM image (Figure 5b) reveals well-resolved lattice fringes with two distinct interplanar spacings. The fringe with a spacing of 0.294 nm is indexed to the (103) crystal plane of $Bi_2O_2CO_3$, while the fringe with a spacing of 0.205 nm corresponds to the (015) crystal plane of

metallic Bi [34]. The close proximity of these two lattice fringes within the same particle or adjacent nanosheets indicates intimate contact between the BCO phase and the Bi nanoparticles, forming a coherent Bi/BCO heterointerface. Such an interface is likely to play a crucial role in electrocatalytic activity, as it may facilitate electron transfer and provide unique adsorption sites for reaction intermediates. The selected area electron diffraction (SAED) pattern exhibits ring patterns, confirming the polycrystalline nature of the sample (Figure S2).

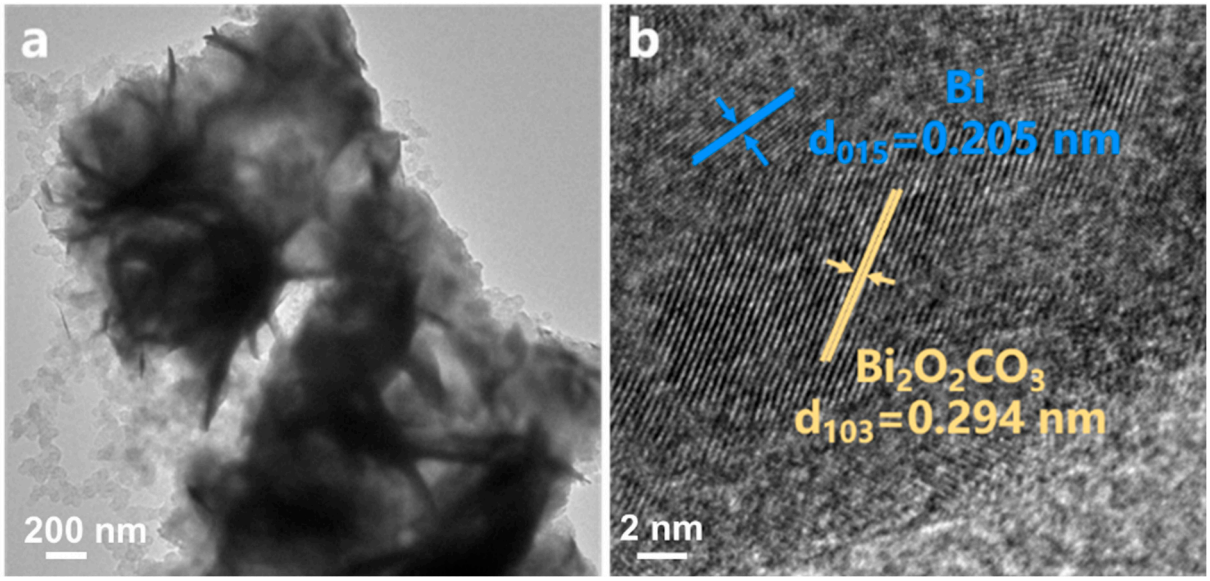

Figure 5. (**a**) TEM image and (**b**) HRTEM image of activated 20%-BCO/BSO.

The surface chemical composition and valence states of the activated 20%-BCO/BSO catalyst were investigated by XPS, as presented in Figure 6. The survey spectrum (Figure 6a) clearly shows the presence of Bi, O, and C elements, while no signal corresponding to sulfur (S) is detected, confirming the complete removal of sulfate groups during the electrochemical activation. This observation is fully consistent with the XRD results, further corroborating the phase transformation from BSO to BCO. The high-resolution Bi 4f spectrum (Figure 6b) exhibits two prominent peaks at binding energies of 159.8 eV and 165.1 eV, which are assigned to the Bi $4f_{7/2}$ and Bi $4f_{5/2}$ spin-orbit components, respectively, which are characteristic of Bi^{3+} in an oxide or carbonate environment [21]. Notably, no obvious peaks attributable to metallic Bi^0 (which would appear at approximately 157.0 eV and 162.3 eV) are observed in the Bi 4f spectrum, despite the detection of metallic Bi by XRD and HRTEM. This apparent discrepancy may be explained by several factors: (i) the metallic Bi nanoparticles are predominantly embedded within the BCO matrix or located at the interface, thus not exposed to the surface within the XPS probing depth; (ii) the metallic Bi species are readily oxidized upon exposure to air during sample transfer, forming a thin Bi_2O_3 overlayer; or (iii) the concentration of metallic Bi at the outermost surface is below the detection limit of XPS. The O 1s spectrum (Figure 6c) can be deconvoluted into three distinct peaks at 529.8 eV, 531.0 eV, and 532.0 eV. The peak at 529.8 eV is assigned to the lattice oxygen in the Bi–O bonds of the BCO structure [26]. The peak at 531.0 eV is characteristic of the oxygen atoms within the carbonate (CO_3^{2-}) groups, which is a fingerprint of the BCO phase. The peak at 532.0 eV is attributed to surface-adsorbed hydroxyl species (-OH) or chemisorbed water, which are commonly present on oxide surfaces exposed to aqueous electrolytes. The C 1s spectrum (Figure 6d) displays two components: a peak at 284.8 eV, which corresponds to adventitious carbon from the environment, and a peak at 288.6 eV,

which is assigned to the carbon-oxygen bonds within the carbonate groups of BCO. This latter peak provides additional confirmation of the BCO structure.

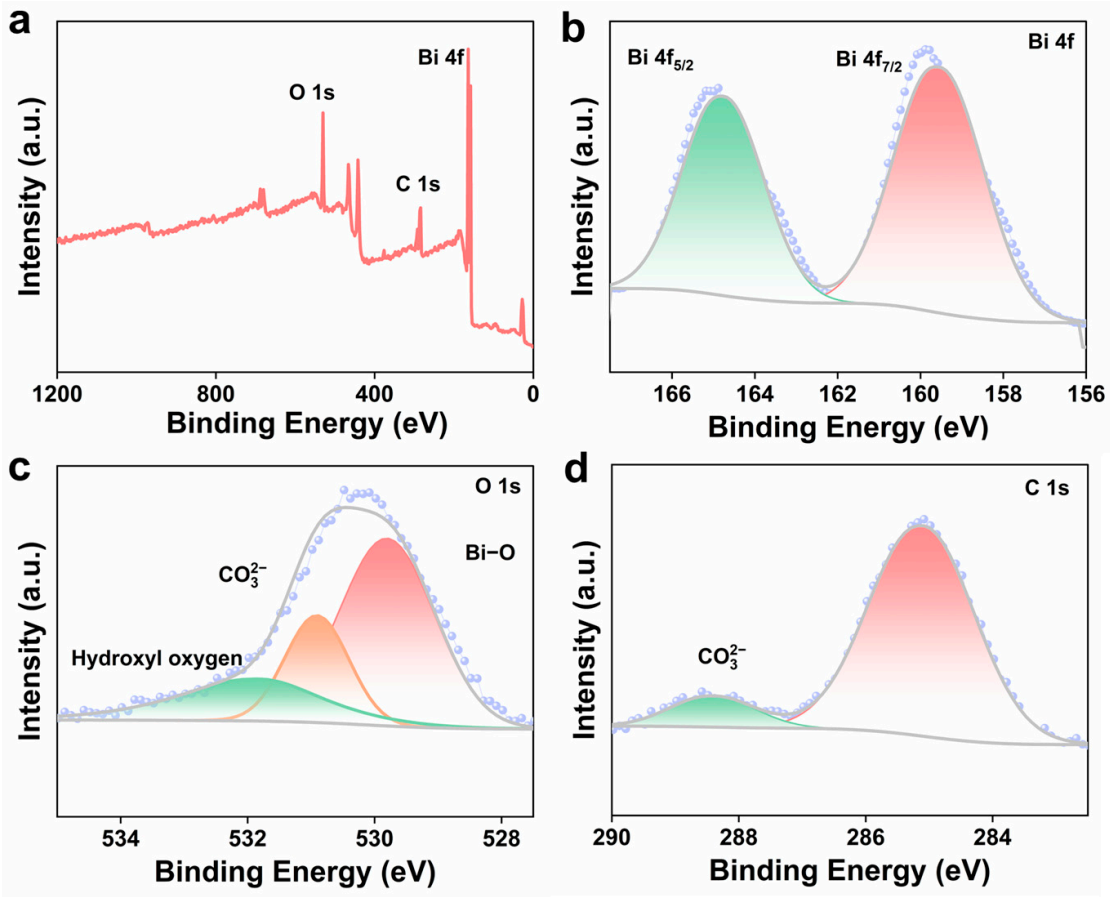

Figure 6. XPS spectra of activated 20%-BCO/BSO: (**a**) survey spectrum, (**b**) Bi 4f, (**c**) O 1s, and (**d**) C 1s.

2.3. Electrochemical Performance and Product Selectivity

The electrochemical properties of the activated BCO/BSO heterojunction catalysts were systematically evaluated using CV, EIS, and LSV. The CV curves recorded in the potential range of 1 to −0.5 V vs. RHE (Figure 7a) exhibit a distinct cathodic peak between 0 and 0.5 V for all heterojunction samples, which is attributed to the reduction of surface Bi^{3+} species to metallic Bi^0. The intensity of this reduction peak decreases with increasing BCO content in the heterojunction. Electrochemical impedance spectroscopy (EIS) measurements were performed to investigate the interfacial charge-transfer behavior of the catalysts. As shown in Figure 7a, all Nyquist plots exhibit depressed semicircle features, indicating the existence of interfacial charge-transfer processes between the catalyst surface and electrolyte. The EIS spectra were fitted using an appropriate equivalent circuit model, and the corresponding fitting parameters are summarized in Table S1. The fitted charge-transfer resistance (R_{ct}) values for BCO, 10% BCO/BSO, 20% BCO/BSO, and 40% BCO/BSO were determined to be 2391, 9677, 4811, and 2792 Ω, respectively. The results indicate that the construction of the BCO/BSO heterostructure significantly influences the interfacial charge-transfer behavior. Among the investigated catalysts, BCO and 40% BCO/BSO exhibit relatively lower charge-transfer resistance, whereas 10% BCO/BSO shows the highest interfacial resistance. The Bode plots (Figure S3) were further analyzed to understand the frequency-dependent electrochemical response. All catalysts exhibit similar phase-angle variation trends, suggesting comparable interfacial relaxation processes. The differences in

the relaxation regions indicate that the BCO/BSO heterostructure modifies the interfacial polarization and electron-transfer behavior. It should be noted that the EIS results mainly reflect the interfacial charge-transfer kinetics rather than the intrinsic electrical conductivity of the catalysts. Although 20% BCO/BSO does not possess the lowest Rct value, it exhibits the best CO_2 reduction performance, suggesting that the enhanced catalytic activity is not solely governed by charge-transfer resistance. Considering the dynamic reconstruction behavior of Bi-based catalysts under electrochemical conditions, the superior CO_2RR performance of 20% BCO/BSO is mainly attributed to the formation of favorable reconstructed Bi/BCO active structures, optimized adsorption of key intermediates, and synergistic effects at the BCO/BSO interface. LSV in Ar-saturated electrolyte (Figure 7c) shows that the heterojunction catalysts exhibit more positive onset potentials and higher current densities than pristine BSO, suggesting enhanced intrinsic activity. In the CO_2-saturated electrolyte (Figure 7d), all catalysts display increased current densities compared to Ar, confirming their activity toward CO_2RR. The 20%-BCO/BSO sample yields the highest current density, indicating superior electrocatalytic activity [35].

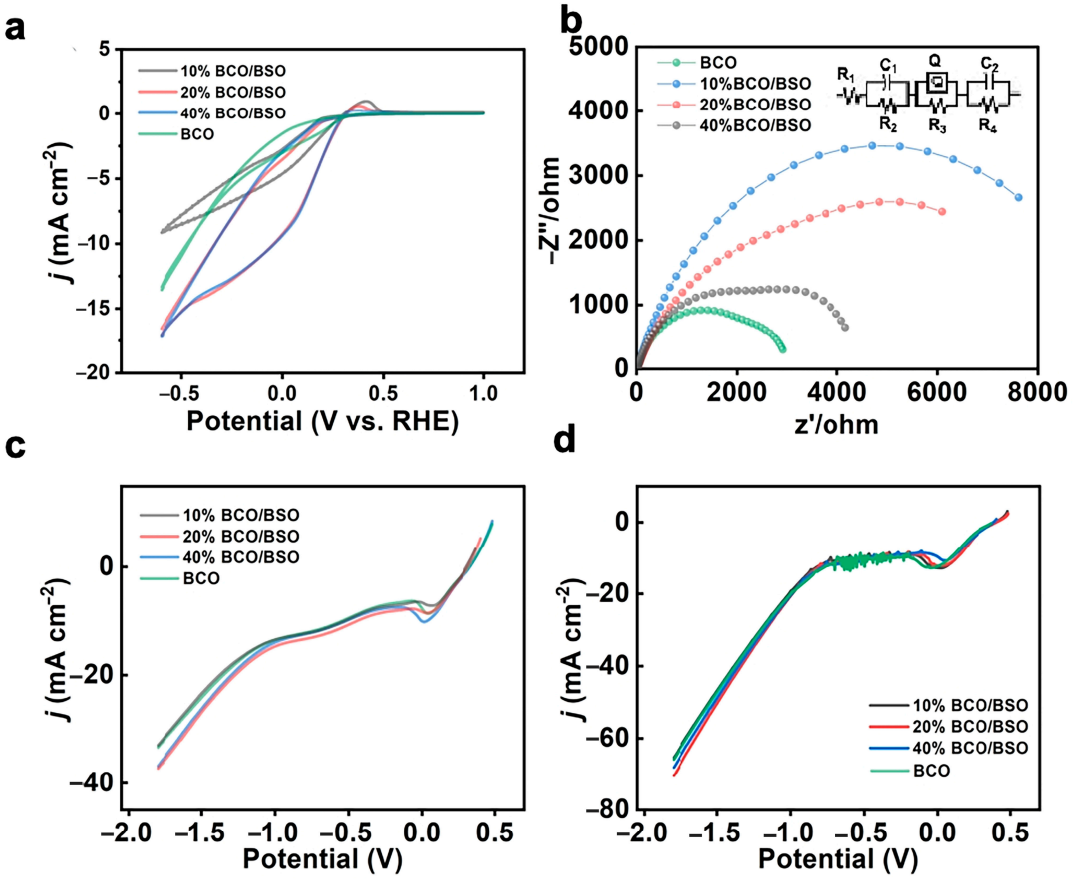

Figure 7. (**a**) CV curves at 50 mV s^{-1}, (**b**) measured and fitted impedance spectrum (Nyquist plots of EIS), and (**c**) LSV in Ar-saturated and (**d**) LSV in CO_2-saturated 0.5 M $KHCO_3$ at 10 mV s^{-1} for different catalysts.

To quantitatively assess the product distribution, controlled-potential electrolysis was carried out at various applied potentials ranging from −1.0 to −1.7 V vs. RHE. The gas-phase products (CO, CH_4, H_2) and liquid-phase products (formate) were analysed by online GC and ion chromatography, respectively. The Faradaic efficiencies (FEs) for each product are summarised in Figure 8. Across all heterojunction catalysts, formate is the dominant product, with FE_{HCOOH} exceeding 80% throughout the entire potential range. The 20%-BCO/BSO catalyst achieves the highest formate Faradaic efficiency of 98.4% at −1.2 V vs.

RHE, corresponding to a formate partial current density of 36.5 mA cm^{-2}, outperforming most state-of-the-art Bi-based catalysts in terms of both selectivity and operational stability (Table S2) [36–45]. Notably, this catalyst maintains FE_{HCOOH} above 95% over a broad potential window from −0.8 to −1.7 V, demonstrating exceptionally stable selectivity despite varying applied potentials. In contrast, the 10%-BCO/BSO and 40%-BCO/BSO catalysts exhibit slightly lower formate FEs, especially at the less negative potentials. The pristine BCO catalyst shows the lowest formate selectivity, with FE_{HCOOH} dropping to below 80% at −1.0 V. The evolution of CO and H_2 as minor products accounts for the remaining Faradaic efficiency, with CO being more prominent at less negative potentials and H_2 increasing at more negative potentials due to the enhanced HER. The long-term stability and durability of bismuth-based electrocatalysts have been systematically investigated in our previous work, where a formate Faradaic efficiency above 90% was maintained even after 900 min of continuous operation at 300 mA cm^{-2} [27].

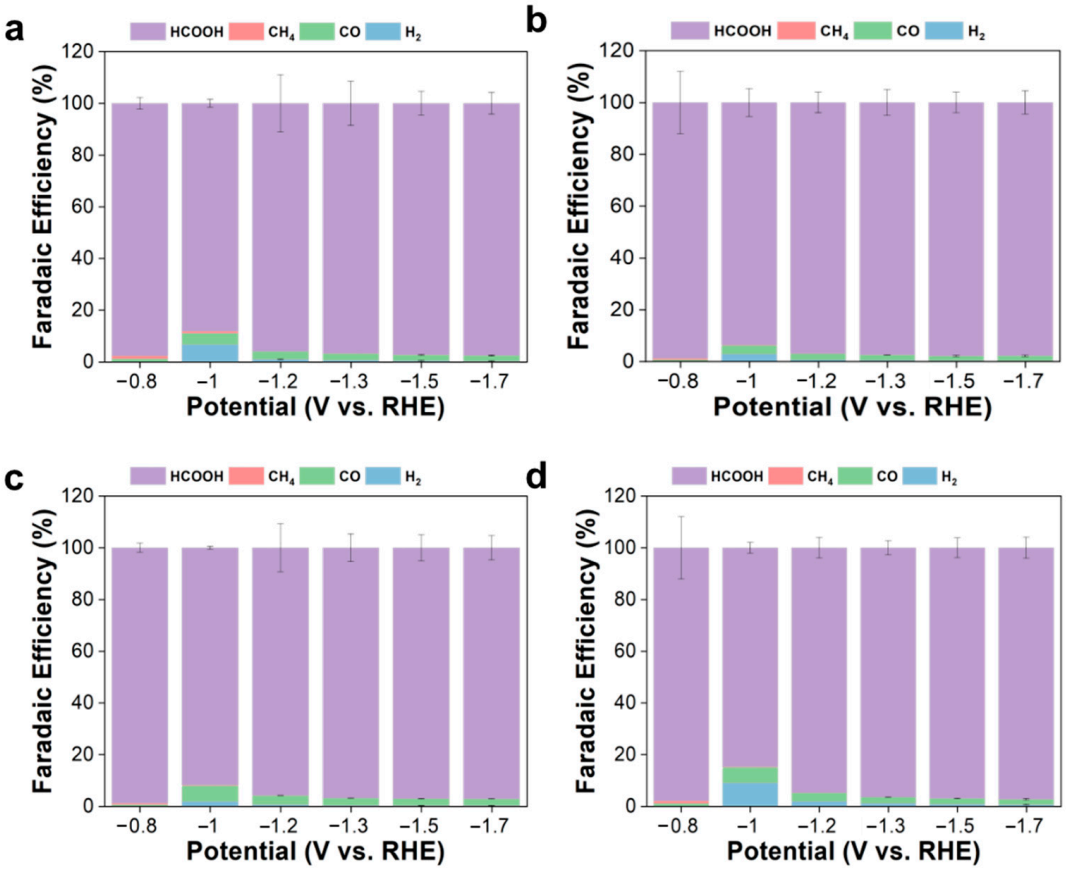

Figure 8. Faradaic efficiencies of formate, CO, and H_2 over (**a**) 10%-, (**b**) 20%-, (**c**) 40%-BCO/BSO, and (**d**) pristine BCO catalysts at different applied potentials.

The superior performance of the 20%-BCO/BSO catalyst can be attributed to several synergistic factors. First, the optimal BCO loading provides a sufficient amount of the BCO phase to stabilize the structure and offer abundant active sites, while retaining enough BSO-derived metallic Bi to create a favourable Bi/BCO interface. Second, the pre-activation step completes the reconstruction to a highly porous nanosheet architecture, maximizing the electrochemically active surface area and facilitating mass transport. Third, the intimate contact between Bi nanoparticles and the BCO matrix at the heterointerface promotes efficient charge transfer and provides unique adsorption configurations for reaction intermediates, as will be discussed in detail in the following section.

2.4. In Situ FTIR Test

To elucidate the reaction pathway and identify the key intermediates responsible for the high formate selectivity, in situ, attenuated, total reflectance Fourier-transform infrared (ATR-FTIR) spectroscopy was performed on the activated 20%-BCO/BSO catalyst during CO_2RR at varying applied potentials (Figure 9). The spectra were recorded in the range of 600–2800 cm^{-1}, where characteristic vibrational modes of key intermediates are typically observed. At open-circuit potential (OCP), the spectrum shows only the background features of the electrolyte and the catalyst itself. The peak near 2390 cm^{-1} in the infrared spectra is attributed to the adsorption of CO_2. The rapid decrease in its intensity with applied potential indicates the progression of the CO_2 reduction process [12]. As the potential is changed to increasingly negative values, several distinct spectral features emerge and intensify.

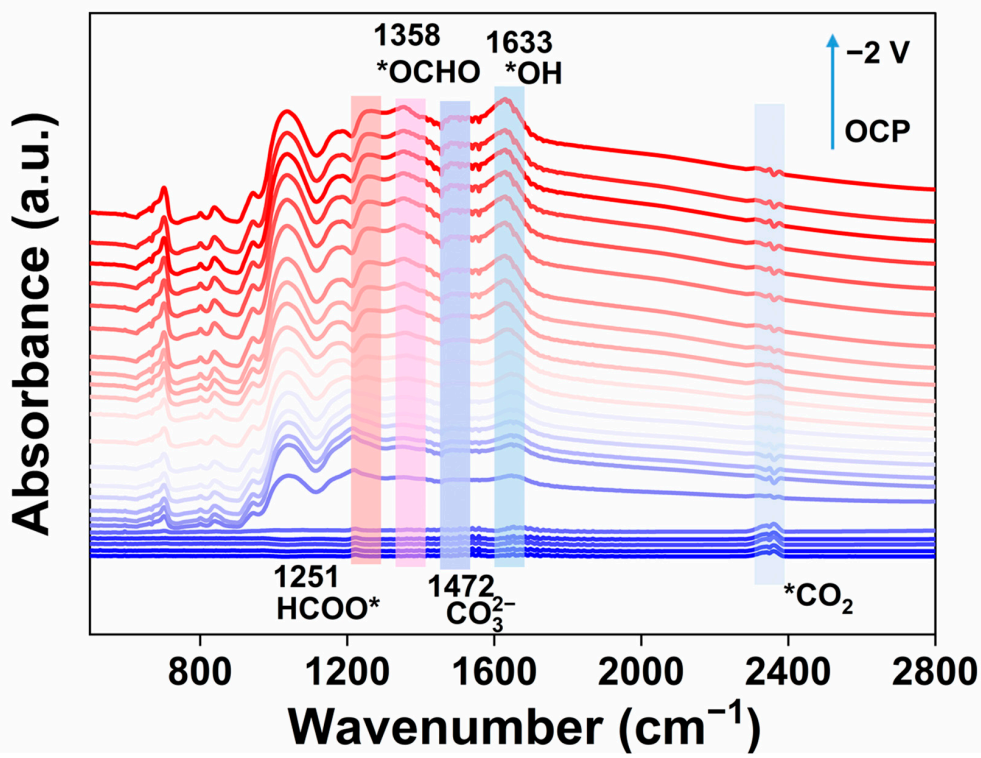

Figure 9. In situ ATR-FTIR spectra of activated 20%-BCO/BSO recorded at applied potentials.

Importantly, no peaks are observed at approximately 2000 cm^{-1} or 2160 cm^{-1}, regions that would correspond to the stretching vibration of adsorbed *CO species. This observation is consistent with the negligible CO Faradaic efficiency measured in the product analysis, confirming that the *CO pathway is not favoured in this catalyst. Instead, a prominent peak appears at 1358 cm^{-1} with increasing cathodic potential, which is assigned to the symmetric stretching vibration of the *OCHO intermediate—a key species formed by the first proton-coupled electron transfer to CO_2 at the oxygen site. The intensity of this peak grows monotonically with an increasingly negative potential, indicating that more *OCHO species accumulated on the catalyst's surface under higher overpotentials [46]. This trend correlates well with the increasing formate production rate observed in the electrochemical measurements. The peak at 1633 cm^{-1} is attributed to the bending vibration (O–H) of adsorbed water molecules in the aqueous electrolyte. The peak at 1472 cm^{-1} is assigned to the asymmetric stretching vibration of carbonate (CO_3^{2-}) species adsorbed on the catalyst surface, which may originate from the electrolyte or from the BCO structure itself. More significantly, a distinct peak at 1251 cm^{-1}, corresponding to adsorbed HCOOH, becomes

visible at potentials more negative than −1.2 V [47]. The intensity of this peak increases with potential, consistent with the enhanced formate production. The observation of both OCHO and HCOOH species suggests that the reaction proceeds via the *OCHO pathway: CO_2 is first adsorbed on the catalyst surface, then hydrogenated to OCHO, followed by a second proton-electron transfer to form HCOOH, which is subsequently desorbed as formate [48]. The absence of *CO-related peaks and the presence of *OCHO peaks are strong evidence that the Bi/BCO interface selectively stabilizes the oxygen-bound intermediate over the carbon-bound *COOH intermediate, thus channelling the reaction towards formate rather than CO.

3. Experimental Section

3.1. Reagents and Materials

All chemical reagents used in this work were of analytical grade and employed without further purification. The main reagents included bismuth nitrate pentahydrate ($Bi(NO_3)_3{\cdot}5H_2O$), isopropanol, potassium bicarbonate ($KHCO_3$), sodium carbonate (Na_2CO_3), methanol, thiourea, and anhydrous ethanol, all purchased from Shanghai Aladdin Biochemical Technology Co., Ltd., Shanghai, China and Sinopharm Chemical Reagent Co., Ltd., Shanghai, China. Carbon paper was obtained from Beijing Chemical Reagents Company, Beijing, China and Nafion solution (5 wt.%) from Shanghai Aladdin, Shanghai, China. Deionized water (18.2 MΩ·cm) was produced using an ultrapure water system. High-purity CO_2 (≥99.99%) and Ar (≥99.99%) gases were supplied by Huzhou Jingcheng Gas Co., Ltd., Huzhou, China.

3.2. Synthesis of BSO Precursor and BCO/BSO Heterojunctions

The BSO precursor was synthesized following a previously reported method [26]. In a typical procedure, 0.57 g (7.5 mmol) of thiourea (CH_4N_2S) was placed in a beaker and dissolved in 60 mL of anhydrous ethanol (C_2H_5OH) under ultrasonication to ensure complete dissolution. Separately, 0.97 g (2 mmol) of bismuth nitrate pentahydrate ($Bi(NO_3)_3{\cdot}5H_2O$) was thoroughly ground in a mortar to obtain a fine and homogeneous powder. The resulting powder was then introduced into the thiourea solution, and the mixture was subjected to further ultrasonication for 20 min to promote enough contact and complexation between the reactants. During this process, a bright-yellow precipitate was formed. The precipitate was collected by centrifugation, washed repeatedly with anhydrous ethanol, and dried. Subsequently, the dried product was placed in a muffle furnace and calcined at 500 °C for 3 h with a heating rate of 2 °C·min^{-1} from room temperature. The final product was designated as BSO.

For the heterojunction preparation, 1.09 g (2 mmol) of the as-prepared BSO powder was dispersed in 100 mL of deionized water under ultrasonication for 15 min to ensure homogeneous dispersion. The suspension was transferred to a water-bath vessel and heated to 50 °C under continuous magnetic stirring. Meanwhile, 0.1 M Na_2CO_3 solution was freshly prepared. Aliquots of 2, 4, 8, and 20 mL of the Na_2CO_3 solution were added dropwise to the BSO suspension over a period of 10 min under vigorous stirring. The reaction was maintained at 50 °C for 30 min to allow enough ion-exchange. After cooling to room temperature and standing for 1 h, the precipitates were collected by centrifugation, washed three times with deionized water and once with ethanol, and then dried at 60 °C overnight. The obtained catalysts were designated as 10%-BCO/BSO, 20%-BCO/BSO, 40%-BCO/BSO, and pristine BCO (from the 20 mL addition). A schematic illustration of the synthesis is shown in Figure 10.

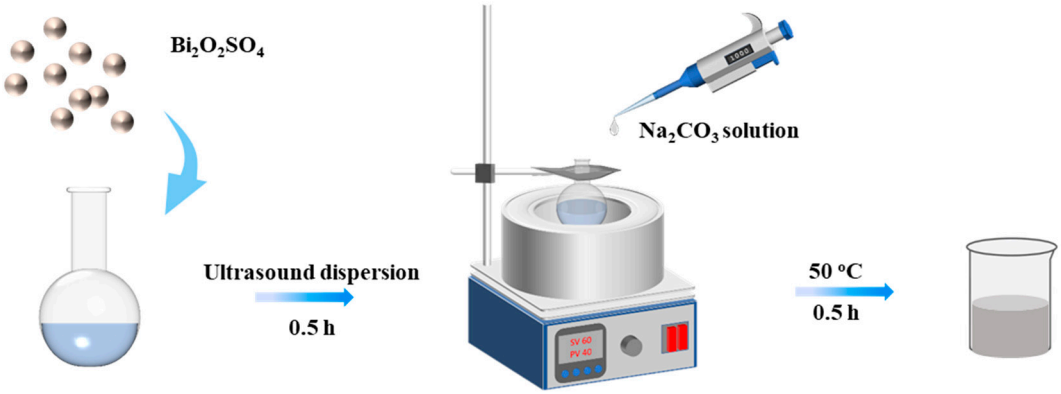

Figure 10. Schematic diagram of the preparation process for BCO/BSO heterojunction catalysts via in situ ion-exchange.

3.3. Physicochemical Characterisation

Crystal structures and phase compositions were determined by X-ray diffraction (XRD, D8 Advance, Bruker, Billerica, MA, USA) using Cu Kα radiation (λ = 0.154 nm) at 40 kV and 40 mA. Data were collected in continuous scanning mode over 2θ = 10–90° at a scan rate of 10° min^{-1}. Surface elemental compositions and chemical states were analysed by X-ray photoelectron spectroscopy (XPS, ESCALAB 250Xi, Thermo Fisher, Waltham, MA, USA) with monochromatic Al Kα radiation. Fourier-transform infrared (FT-IR) spectra were recorded on a Vertex 80 V spectrometer (Bruker) in transmission mode over 40–4000 cm^{-1}, using KBr pellets as the background. The morphology of the catalysts was examined by scanning electron microscopy (SEM, Hitachi S-4800H, Tokyo, Japan) with an accelerating voltage of 15 kV. Transmission electron microscopy (TEM) and high-resolution TEM (HRTEM) were performed on a JEOL JEM-2100F microscope (Tokyo, Japan) operated at 200 kV, equipped with energy-dispersive X-ray spectroscopy (EDS) for elemental mapping.

3.4. Electrochemical Measurements

All electrochemical tests were conducted in a gas-tight flow-type electrolytic cell (Gaoshiruilian Company, Tianjin, China, as shown in Figure S4) with the cathodic and anodic compartments separated by a Nafion 115 proton exchange membrane (Shanghai Aladdin, Shanghai, China) to prevent product crossover. The working electrode was prepared by spray-coating a catalyst ink onto carbon paper (geometric area = 1 cm^2). The ink formulation consisted of 50 mg of catalyst, 150 μL of Nafion solution, 7.5 mL of isopropanol, and 2.5 mL of deionized water, ultrasonically mixed for 30 min. An IrO_2-Ta_2O_5/Ti mesh (100 mesh, 1 cm^2 projected area) and an Ag/AgCl electrode served as the counter and reference electrodes, respectively. All measured potentials were calibrated to the reversible hydrogen electrode (RHE) scale using the equation: $E_{RHE} = E_{Ag/AgCl} + 0.0591 \times pH + 0.197$.

The anode and cathode reactions are as follows:

$$\text{Cathode: } CO_2 + H_2O + 2e^- \rightarrow HCOO^- + OH^-$$

$$\text{Anode: } 2H_2O \rightarrow O_2 + 2H^+ + 4e^-$$

The pre-activation process: Prior to the formal CO_2 reduction tests, the working electrodes were electrochemically activated by cyclic voltammetry (CV) between 0.3 and −1.3 V vs. RHE at 50 mV s^{-1} in CO_2-saturated 0.5 M $KHCO_3$ until stable CV curves were obtained (typically 20 cycles). This pre-activation step was designed to complete

the structural reconstruction before the long-term stability and performance tests. Linear sweep voltammetry (LSV) was performed at a scan rate of 10 mV s^{-1} in both Ar- and CO_2-saturated 0.5 M $KHCO_3$ over the potential range of −0.4 to −2.5 V vs. RHE. Electrochemical impedance spectroscopy (EIS) was recorded from 0.01 Hz to 100 kHz with an AC amplitude of 5 mV at open-circuit potential. All electrochemical measurements were conducted using a CHI 760E electrochemical workstation.

Constant-potential electrolysis was carried out at various applied potentials (−1.0 to −1.7 V vs. RHE) under a continuous CO_2 flow (10 sccm) maintained by a mass flow controller. Gas-phase products (CO, CH_4, H_2) were analysed online by gas chromatography (GC9800, Shanghai Kechuang Co., Ltd., Shanghai, China,) equipped with a flame ionization detector (FID) and a thermal conductivity detector (TCD), using TDX-01 and GDX-502 columns. Liquid-phase products (formate, acetate) were quantified by ion chromatography (ICO IC, Metrohm, Herisau, Switzerland) after 10-fold dilution with ultrapure water. The Faradaic efficiency (FE) for each product was calculated from the total charge passed and the molar amount of product formed, with equations provided in the Supplementary Information.

4. Conclusions

In summary, we systematically investigated the reconstruction behaviour of bismuth-based electrocatalysts for CO_2 reduction, revealing that BSO undergoes complete conversion to BCO nanosheets with partial reduction to metallic Bi^0 under cathodic potentials. To circumvent the detrimental effects of uncontrolled reconstruction, we devised a pre-activation strategy that deliberately completes the structural evolution prior to electrolysis, effectively stabilising the catalyst. A series of BCO/BSO heterojunction catalysts were synthesised via a mild in situ ion-exchange method, and the optimised 20%-BCO/BSO achieved a remarkable Faradaic efficiency of 98.4% for formate at −1.2 V vs. RHE, with >95% FE over a wide potential window. In situ ATR-FTIR spectroscopy identified that the reconstructed interface can stabilise the *OCHO intermediate and promote formate production while suppressing the *CO pathway. This work not only elucidates the reconstruction mechanism but also demonstrates that controlled reconstruction, through pre-activation, can be harnessed as a beneficial strategy for achieving stable and efficient CO_2 electroreduction, offering a promising approach for the rational design of durable electrocatalysts.

Supplementary Materials: The following supporting information can be downloaded at: https://www.mdpi.com/article/10.3390/catal16080725/s1. Figure S1. SEM image of BSO; Figure S2. The selected area electron diffraction (SAED) pattern of activated 20%-BCO/BSO; Figure S3. (a) Bode magnitude plots, and (b) Bode phase angle plots for different catalysts; Figure S4. the actual flow-cell reactor and a schematic diagram; Table S1. Equivalent circuit fitting parameters of EIS spectra for BCO and BCO/BSO catalysts; Table S2. Comparison of electrocatalytic CO_2-to-formate performance over state-of-the-art Bi-based catalysts in recent years.

Author Contributions: H.X.: conceptualization and writing of the original manuscript. L.Y.: investigation, experimentation, conceptualization, and formal analysis. S.L.: data analysis and review. P.X.: experimentation, editing, and formal analysis. D.L.: editing and review. L.W.: conceptualization, investigation, and review and editing. All authors have read and agreed to the published version of the manuscript.

Funding: This work was funded by the National Natural Science Foundation of China (No. 22576030), Joint Fund of the Zhejiang Provincial Natural Science Foundation of China (No. LBMHY25E060009) and Public Welfare Application Research Project of Huzhou (2023GZ07).

Data Availability Statement: The data that support the findings of this study are available from the corresponding authors upon reasonable request.

Conflicts of Interest: The authors declare no conflicts of interest.

References

1. Bassett, K.R.; Hupperts, S.F.; Jämtgård, S.; Östlund, L.; Fridman, J.; Perakis, S.S.; Gundale, M.J. Rising Atmospheric CO2 Reduces Nitrogen Availability in Boreal Forests. *Nature* **2026**, *650*, 629–635. [CrossRef] [PubMed]
2. Zhou, X.; Liu, Y.; Liu, L.; Yu, Y.; Xu, J.; Ruan, M.; Li, S.; Qian, L. Unveiling and Utilizing the Reconstructing Dynamics on Nanoporous Ag-Bi for CO2 Electroreduction. *Appl. Catal. B* **2024**, *343*, 123552. [CrossRef]
3. Lee, C.-H.; Subhas, A.V.; Kim, J.-H.; Lee, K. Ocean Carbon Dioxide Removal and Storage. *Chem. Rev.* **2026**, *126*, 1110–1144. [CrossRef] [PubMed]
4. Zheng, H.; Yang, Z.; Luo, L.; Cheng, J.; Jin, Y.; Gao, Q.; Fan, M.; Zhao, Z.; Kong, X.; Zhang, X.; et al. Engineering the Stable BiO5 Species for Efficient Electrodirection of CO2 into Formic Acid at Ampere-Level Current. *Nano Lett.* **2025**, *25*, 8750–8757. [CrossRef] [PubMed]
5. Hong, Y.; Zhou, X.; Zeng, F. Integrating Carbon-Coated Cu/Cu2O Nanoparticles with Biochars Enabled Efficient Capture and Electrocatalytic Reduction of CO2. *Catalysts* **2025**, *15*, 767. [CrossRef]
6. Li, Z.; Choy, K.L. Ternary SiO2@CuO/g-C3N4 Nanoparticles for Solar-Driven Photoelectrocatalytic CO2-to-Fuel Conversion. *Catalysts* **2025**, *15*, 892. [CrossRef]
7. Li, J.; Li, D.; Liu, S.; Su, J.; Chen, L. Recent Progress in the Moderation Strategies of Bi-precatalyst Reconstruction for Electrocatalytic CO2 Reduction to Formate. *Adv. Synth. Catal.* **2026**, *368*, e70271. [CrossRef]
8. Rhi, S.; Park, S.; Heo, D.Y.; Iimura, S.; Kim, S.Y. Selective Electroreduction of CO2 to Ethanol: Mechanistic Understanding and Catalyst Development. *MetalMat* **2026**, *3*, e70024. [CrossRef]
9. Deng, B.; Huang, M.; Li, K.; Zhao, X.; Geng, Q.; Chen, S.; Xie, H.; Dong, X.a.; Wang, H.; Dong, F. The Crystal Plane Is Not the Key Factor for CO2-to-Methane Electrosynthesis on Reconstructed Cu2O Microparticles. *Angew. Chem. Int. Ed.* **2022**, *61*, e202114080. [CrossRef] [PubMed]
10. Lu, X.; Wang, L.; Xie, H.; Li, Z.; Du, X.; Deng, B. Ge4+ Stabilizes Cu+ Active Sites to Synergistically Regulate the Interfacial Microenvironment for Electrocatalytic CO2 Reduction to Ethanol. *Appl. Sci.* **2025**, *15*, 11420. [CrossRef]
11. Ma, W.; Xie, S.; Liu, T.; Fan, Q.; Ye, J.; Sun, F.; Jiang, Z.; Zhang, Q.; Cheng, J.; Wang, Y. Electrolytic Reduction of CO2 to Ethylene and Ethanol through Hydrogen-Assisted C-C Coupling over Fluorine-Modified Copper. *Nat. Catal.* **2020**, *3*, 478–487. [CrossRef]
12. Xiang, P.; Wang, L.; Geng, Q.; Guo, C.; Xie, H.; Li, Y.; Yu, Y.; Wang, J. Improvement of Efficiency and Selectivity of CO2 Photoreduction over Bi2O2SO4 Catalysts with Cu-Bi Alloys. *Surf. Interfaces* **2025**, *62*, 106192. [CrossRef]
13. Khan, B.; Cheng, Y.-T.; He, J.-H. Engineering Strategies toward Scalable CO2-to-Liquid-Fuel Photoelectrolysis. *Joule* **2026**, *10*, 102529. [CrossRef]
14. Deng, X.; Li, R.; Wu, S.; Wang, L.; Hu, J.; Ma, J.; Jiang, W.; Zhang, N.; Zheng, X.; Gao, C.; et al. Metal-Organic Framework Coating Enhances the Performance of Cu2O in Photoelectrochemical CO2 Reduction. *J. Am. Chem. Soc.* **2019**, *141*, 10924–10929. [CrossRef] [PubMed]
15. Wang, P.; Yang, H.; Tang, C.; Wu, Y.; Zheng, Y.; Cheng, T.; Davey, K.; Huang, X.; Qiao, S.Z. Boosting Electrocatalytic CO2-to-Ethanol Production via Asymmetric C-C Coupling. *Nat. Commun.* **2022**, *13*, 3754. [CrossRef] [PubMed]
16. Zhang, Y.; Pan, D.; Tao, Y.; Shang, H.; Zhang, D.; Li, G.; Li, H. Photoelectrocatalytic Reduction of CO2 to Syngas via SnOx-Enhanced Cu2O Nanowires Photocathodes. *Adv. Funct. Mater.* **2022**, *32*, 2109600. [CrossRef]
17. Chen, C.; Zhang, J.; Qi, Y.; Zhang, J.; Guo, T.; Wang, H. Locust Leaves-Derived Biochar Coupled CuxO Composites for Efficient Electrocatalytic CO2 Reduction. *Fuel* **2024**, *372*, 132245. [CrossRef]
18. Dong, L.; Feng, D.; Zhang, Y.; Wang, Z.; Zhao, Y.; Du, Q.; Gao, J.; Sun, S. Mechanism of Biochar-Cu-Based Catalysts Construction and Its Electrochemical CO2 Reduction Performance. *Carbon Capture Sci. Technol.* **2024**, *13*, 100250. [CrossRef]
19. Yang, Z.; Chen, Y.; Wen, X.; Guo, X.; Wei, R.; Gao, L.; Pan, X.; Zhang, J.; Xiao, G. Modulable Cu(0)/Cu(I)/Cu(II) Sites of Cu/C Catalysts Derived from MOF for Highly Selective CO2 Electroreduction to Hydrocarbons. *Vacuum* **2023**, *215*, 112231. [CrossRef]
20. Zhang, X.; Liang, X.; Yan, H.; Wang, X.; Zhang, Y.; Ji, M.; Wang, M.; Wang, X. Low-Crystallinity-Induced Lattice-Distorted Bismuth Nanosheets for Enhanced Electrocatalytic CO2 Reduction to Formate. *Nano Lett.* **2025**, *25*, 9075–9083. [CrossRef] [PubMed]
21. Li, S.; Zhang, Y.; Qiao, P.; Wu, C.; Tian, X.; Xu, Y.; Zhang, Y.; Wang, P.; Li, T.; Afaq, M.; et al. Efficient Electrocatalytic Conversion of CO2 to Pure Formic Acid Solutions via Strain-Engineered Bismuth Nanosheets. *Adv. Sci.* **2026**, *13*, e75152. [CrossRef] [PubMed]
22. Liang, Z.; Song, L.; Jiang, Y.; Liu, J.; Zhang, Y.; Zhang, Q.; Yan, C.-H.; Du, Y. Penta-Coordinated Y Sites Modulated Single Bi Sites for Promoted Selectivity of Electrochemical CO2 Reduction. *Adv. Funct. Mater.* **2023**, *33*, 2311087. [CrossRef]
23. Lee, C.W.; Hong, J.S.; Yang, K.D.; Jin, K.; Lee, J.H.; Ahn, H.Y.; Seo, H.; Sung, N.E.; Nam, K.T. Selective Electrochemical Production of Formate from Carbon Dioxide with Bismuth-Based Catalysts in an Aqueous Electrolyte. *ACS Catal.* **2018**, *8*, 931–937. [CrossRef]
24. Peralta, C.E.; Abarca, J.A.; Díaz-Sainz, G.; Santos, E.; Irabien, A. Techno-Economic Analysis of a Three-Compartment CO2 Electrolyzer for Formic Acid Production. *ChemSusChem* **2026**, *19*, e202600123. [CrossRef] [PubMed]

25. Abarca, J.A.; Díaz-Sainz, G.; Irabien, A. CO2 Electroreduction to Formate: Advancing toward Scalable Technologies. *ACS Appl. Energy Mater.* **2026**, *9*, 2041–2049. [CrossRef] [PubMed]
26. Geng, Q.; Xie, H.; He, Y.; Sun, Y.; Hou, X.; Zhiming, W.; Dong, F. Atomic Interfacial Structure and Charge Transfer Mechanism on In-Situ Formed BiOI/ Bi2O2SO4 p-n Heterojunctions with Highly Promoted Photocatalysis. *Appl. Catal. B* **2021**, *297*, 120492. [CrossRef]
27. Wang, L.; Deng, B.; Xie, H.; Lu, X.; Xiang, P.; Zhao, X.; Li, Y.; Dong, F. Anion-Regulated Reconstruction of Bismuth-Based Electrocatalysts for Enhanced Electrocatalytic CO2 Reduction. *J. Energy Chem.* **2026**, *113*, 598–609. [CrossRef]
28. Mei, X.; Zhao, X.; Du, H.; Deng, B.; Zhuo, H.; Li, Q.; Zhu, C.; Xie, H.; Cao, Y.; Li, Y.; et al. Adjusting the Active Site of Single Co Atoms on CeO2 via Cyano Functional Groups for Selective H2O2 Electrosynthesis at High Yield. *Appl. Catal. B* **2025**, *374*, 125398. [CrossRef]
29. Chen, Z.; Liu, J.; Wei, Y.; Liu, Y.; Mo, G.; Chen, B.; Zhao, S.; Wu, Z. Recent Advances in Regulation Strategy and Catalytic Mechanism of Bi-Based Catalysts for CO2 Reduction Reaction. *Nano-Micro Lett.* **2026**, *18*, 26. [CrossRef] [PubMed]
30. Yu, W.-B.; Yi, M.; Fu, H.-H.; Pei, M.-J.; Liu, Y.; Xu, B.-M.; Li, Y.; Yan, W.; Zhang, J. Dandelion-Like Nanostructured Cu/Cu2O Heterojunctions with Fast Diffusion Channels Enabling Rapid Photocatalytic Pollutant Removal. *ACS Appl. Nano Mater.* **2023**, *6*, 2928–2941. [CrossRef]
31. Li, F.; Tang, H.; Yang, H.; Cao, Y.; Zhou, T.; Wang, G. Steering Electrochemical CO2 Reduction Selectivity toward CH4 or C2H4 on N-Doped Carbon-Coated Cu/Cu2O Composite Catalysts. *ACS Catal.* **2024**, *14*, 15088–15095. [CrossRef]
32. Hu, R.; Xiao, X.; Tu, S.; Zuo, X.; Nan, J. Synthesis of Flower-Like Heterostructured β-Bi2O3/ Bi2O2CO3 Microspheres Using Bi2O2CO3 Self-Sacrifice Precursor and Its Visible-Light-Induced Photocatalytic Degradation of o-Phenylphenol. *Appl. Catal. B* **2015**, *163*, 510–519. [CrossRef]
33. Tao, J.-G.-L.; Wang, D.; Zhao, B.; Chen, F. Bi−O Site Lattice Engineering towards Durable and Efficient CO2 Electroreduction. *Adv. Funct. Mater.* **2026**, *36*, e29954. [CrossRef]
34. Jiao, Z.; Zhang, Y.; Ouyang, S.; Yu, H.; Lu, G.; Ye, J.; Bi, Y. BiAg Alloy Nanospheres: A New Photocatalyst for H2 Evolution from Water Splitting. *ACS Appl. Mater. Interfaces* **2014**, *6*, 19488–19493. [CrossRef] [PubMed]
35. Jiang, Z.; Ren, S.; Cao, X.; Fan, Q.; Yu, R.; Yang, J.; Mao, J. pH-Universal Electrocatalytic CO2 Reduction with Ampere-Level Current Density on Doping-Engineered Bismuth Sulfide. *Angew. Chem. Int. Ed.* **2024**, *63*, e202408412. [CrossRef] [PubMed]
36. Chen, Q.; Kube, A.; Kopljar, D.; Friedrich, K.A. Advanced impedance analysis for performance degradation during low-temperature CO2 electroreduction. *ACS Energy Lett.* **2024**, *9*, 6096–6103. [CrossRef]
37. Xia, Y.; Li, Y.; Liu, X.; Liu, S.; Jiao, X. Steering Ce Atoms as an Electronic Reservoir in Tpy-Regulated Bi2Te3 Nanosheets for Enhanced CO2 Reduction to Formate. *Chem. Eng. J.* **2026**, *538*, 176957. [CrossRef]
38. Wang, Y.; Wang, Z.; Yi, S.; Zhang, Q.; Ji, M.; Yang, J.; Yan, P.; Zhu, X.; Xu, H.; She, X. Hierarchical Bi/Bi2O3 Heterostructures with Robust Oxygen Vacancies for Efficient Electrochemical CO2 Reduction to Formate. *Chem. Commun.* **2025**, *61*, 18140–18143. [CrossRef] [PubMed]
39. Zhang, C.; Zhong, Y.; Wang, X.; Chen, Y.; Jiang, C.; Majozi, T.; Wang, Z.; Karadas, F. Ce Doping-Induced Abundant Bi–O Species on Metallic Bismuth for Electrochemical CO2 Reduction to Formic Acid. *J. Mater. Sci. Technol.* **2025**, *254*, 258–266. [CrossRef]
40. Ren, X.; Gong, S.; Han, Z.; Wei, Y.; Gao, Y. Stabilizing Bi Active Species via Constructing a Bi–O–Ce Interface for Enhanced CO2 Electroreduction to Formate. *Chem. Commun.* **2026**, *62*, 3915–3919. [CrossRef] [PubMed]
41. Fan, F. Boosting Electrocatalytic CO2 Reduction by Sulfur-Modified Bismuth Nanosheets. *J. Phys. Conf. Ser.* **2025**, *3112*, 012078. [CrossRef]
42. Arndt, B.M.; Phillips, A.; Valdez Arriaran, D.; Nazemi, R. Electronic Modulation of Bismuth Active Sites in Bimetallic Zeolitic Imidazolate Frameworks Enables Selective CO2 Electroreduction in a Bipolar Membrane Flow Cell. *ACS Appl. Energy Mater.* **2026**, *9*, 10054–10065. [CrossRef]
43. Ma, A.; Lee, Y.; Seo, D.; Kim, J.; Park, S.; Son, J.; Kwon, W.; Nam, D.H.; Lee, H.; Kim, Y.I.; et al. Unlocking the Potential of Bi2S3-Derived Bi Nanoplates: Enhanced Catalytic Activity and Selectivity in Electrochemical and Photoelectrochemical CO2 Reduction to Formate. *Adv. Sci.* **2024**, *11*, 2400874. [CrossRef] [PubMed]
44. Fayaz, A.; Varghese, A.M.; Dey, G.; Kumar, R.; Sampath, S. Two-Dimensional BiPS4-Derived Catalyst for the Selective Electroreduction of CO2: The Synergistic Effect of Phosphorus and Sulfur along with Bismuth. *ACS Appl. Energy Mater.* **2026**, *94*, 2172–2183. [CrossRef]
45. Choi, S.Y.; Liu, Y.; Woo, C.; Choi, Y.; Kang, W.J.; Oh, H.-S.; Baik, J.M. Structurally and Electronically Coupled Bi/Bi3Ni–Carbon Dot Catalyst for Efficient and Long-Lived CO2 Electroreduction to Formate. *Nano Energy* **2026**, *30*, 111690. [CrossRef]
46. Yang, X.; Yuan, Q.; Sheng, T.; Wang, X. Mesoporous Mo-Doped PtBi Intermetallic Metallene Superstructures to Enable the Complete Electrooxidation of Ethylene Glycol. *Chem. Sci.* **2024**, *15*, 4349–4357. [CrossRef] [PubMed]

47. Yang, X.; Yuan, Q.; Sheng, T.; Wang, X. Electrocatalytic CO2 and HCOOH Interconversion on Pd-Based Catalysts. *Adv. Sens. Energy Mater.* **2022**, *1*, 100007. [CrossRef]
48. Rakić, V.M.; Hercigonja, R.V.; Dondur, V.T. CO Interaction with Zeolites Studied by TPD and FTIR: Transition-Metal Ion-Exchanged FAU-Type Zeolites. *Microporous Mesoporous Mater.* **1999**, *27*, 27–39. [CrossRef]